Unlocking the charge efficiency of γ'-V2O5 for Na-ion battery through a solution synthesis technique

Dauren Batyrbekuly, Barbara Laïk, Zhumabay Bakenov, Ankush Bhatia, Jean-Pierre Pereira-Ramos, Rita Baddour-Hadjean

Unlocking the charge efficiency of γ'-V_2O_5 for Na-ion battery through a solution synthesis technique

Dauren Batyrbekuly[1,2], Barbara Laïk[1], Zhumabay Bakenov[2], Ankush Bhatia[1], Jean-Pierre Pereira-Ramos[1], Rita Baddour-Hadjean*[1]

[1] Univ. Paris Est Créteil, CNRS, ICMPE, UMR 7182, 2 rue Henri Dunant, 94320 Thiais, France
[2]School of Engineering, National Laboratory Astana, Nazarbayev University, 53 Kabanbay Batyr Avenue, Astana 010000, Kazakhstan

*Corresponding author: rita.baddour-hadjean@cnrs.fr; Tel: 33 1 49 78 11 55

ABSTRACT

In this study, the γ'-V_2O_5 cathode material was prepared through a solution synthesis technique leading to homogeneous, fine and porous particles 100-200 nm in size. This successful preparation allows to overcome the huge drawback of the microsized material in terms of charge efficiency and to take benefit of the attractive Na insertion properties of γ'-V_2O_5, i. e. a significant available capacity of 145 mAh g^{-1}, a high working potential of about 3.25 V vs. Na^+/Na, an excellent charge efficiency, a high-rate capability and good cycle life. A detailed structural study upon Na insertion/extraction shows that the proposed nanosizing approach promotes a homogeneous Na solubility and solid solution behavior in a wider composition range ($0.4 < x \leq 1$ in γ-$Na_xV_2O_5$) compared to the results previously reported for solid-state synthesized γ'-V_2O_5. Furthermore, highly reversible structural changes are evidenced. Key kinetic parameters governing the Na insertion-extraction reaction are discussed thanks to an impedance spectroscopy study revealing a faster Na diffusivity in the one-phase region. The obtained results allow a comprehensive understanding of the enhanced performance exhibited by the present sub-micronic γ'-V_2O_5 material.

Keywords: cathode material, V_2O_5, Na-ion battery, impedance spectroscopy

1. INTRODUCTION

Lithium-ion batteries (LIBs) are widely used in various domains including portable electronics like smartphones, laptops, cameras, power tools but can also be found in aerospace, marine and medical applications. Moreover, LIBs are now considered as a key energy storage technology for electric vehicles and are simultaneously evaluated as storage systems for renewable energies. However, large-scale applications of these batteries require cost effectiveness, materials sustainability and environmental friendliness [1]. This success is due to high-energy density of LIBs, a tiny memory effect and low self-discharge. Despite these growth forecasts, considering the low natural presence of lithium in the upper crust and mining and refining expenses, the scientific community is moving towards the discovery of alternative systems to LIBs. This context prompted researchers to transfer the LIBs technology to sodium ion batteries (NIBs), because of sodium low cost, its abundant resource and environmental friendliness [2,3]. Moreover, because sodium ion will not form alloy with aluminum, both positive and negative current collector of NIBs can use cheaper and lighter aluminum instead of copper used in LIBs, which is beneficial from gravimetric cell energy and power density viewpoints. Consequently, and despite a larger radius (0.102 nm vs. 0.076 nm for Na^+ vs. Li^+), a heavier molar mass (22.99 g mol^{-1} vs. 6.94 g mol^{-1} for Na^+ vs. Li^+) and a more positive potential (-2.71 V/ENH vs. -3.04 V/ENH for Na^+ vs. Li^+) causing loss of energy and power density, NIBs have recently gained commercialization status, primarily for stationary energy storage applications, and the market is expected to grow significantly for the forecast period 2022 to 2030 [4]. Based on the intended applications, one of the most challenging problems remains the identification of suitable electrodes materials for NIBs.

Among various candidates as positive electrode materials for NIBs [2,3], layered orthorhombic α- V_2O_5, is worth of interest due to its high theoretical capacity (442 mAh g^{-1} for three exchanged electrons per mole of V_2O_5) and large abundance. Furthermore, it is recognized that the intercalation capacity and cyclability of V_2O_5 can be optimized by playing on its structure, crystallinity, morphology and grain size through different synthesis [5]. Sodium insertion properties of V_2O_5 have been firstly investigated in the late 80s' by West et al. [6] at 80°C with a solid electrolyte and Pereira-Ramos et al. [7] at 150°C in molten dimethylsulfone. Since these pioneering works, few papers have been devoted to the study of the Na electrochemical insertion in this open structure material. A few years ago, our group reported the first room temperature (RT) study of electrochemical Na insertion in V_2O_5 [8]. The

irreversible formation of α'-NaV_2O_5 was demonstrated, followed by a reversible insertion of 0.8 additional Na at a working potential of around 2.0 V (120 mAh g^{-1}) that could be reversibly extracted/inserted over several dozens of cycles. Nano-structuring of the material was also reported as beneficial in terms of capacity and cycling. For instance, V_2O_5 hollow nanospheres were shown to exhibit a capacity of about 150 mAh g^{-1} at 20 mA g^{-1} in the wide 1.0 – 4.2 V potential window, which was retained upon cycling [9].

Another way to increase V_2O_5 electrochemical performance is to consider other polymorphs such as the bilayered ε'-V_2O_5 [10,11] or the γ' variety of V_2O_5 characterized by a puckered layer stacking. Since the earlier study of Cocciantelli et al. reporting the preparation of γ'-V_2O_5 by chemical or electrochemical deintercalation of lithium from the γ-LiV_2O_5 bronze [12], this polymorph has been extensively studied in our group as cathode material in LIBs [13,14] and NIBs [10,15–17]. It is noticeable that one Li^+ per mole of oxide can be reversibly inserted in γ'-V_2O_5, at a higher working potential than α-V_2O_5 (3.55 V vs. Li^+/Li for γ'-V_2O_5 vs. 3.35 V vs. Li^+/Li for α-V_2O_5) [14]. On the other hand, in the case of sodium insertion, γ'-V_2O_5 exhibits one single reduction step with a plateau extending up to ~1 Na^+ per mole of oxide [16]. Remarkably, sodium and lithium insertion take place practically at the same potential in γ'-V_2O_5, at c.a. 3.3 V vs. Na^+/Na (~ 0.6 V vs. NHE). Such result suggests that the original puckered and flexible structure of the γ' polymorph, characterized by a large interlayer spacing (5.02 Å in γ'-V_2O_5 against 4.37 Å in α-V_2O_5), makes Na^+ insertion and diffusion easier.

In our previous papers [10,13–16], γ'-V_2O_5 was prepared from the γ-LiV_2O_5 precursor obtained by carbothermal reduction method at 600°C reported by Barker et al. [18]. The resulting γ'-V_2O_5 material (denoted as γ'-carbo) was shown to exhibit a high discharge rate capability at RT for sodiation with a slight capacity decrease from 145 mAh g^{-1} at C/60 to 135 mAh g^{-1} and 120 mAh g^{-1} at C/2 and 1C, respectively [16]. However, the first charge process was characterized by a low efficiency (53% at C/10) lowering the value of the stable capacity (70 mAh g^{-1} after 70 cycles). A full Na extraction was successfully achieved by applying both a lower C rate (C/60) and a higher cell operating temperature (50 °C), which suggested that the low efficiency of the first cycle was due to a kinetic limitation, probably due to the morphology of the γ'-carbo powder made of platelets of a few micrometers [16]. To overcome this drawback, a ball-milling treatment was applied on γ'-carbo, that led to a decrease of the particle size by a factor 3 without altering the γ'-V_2O_5 structure [10]. This strategy has proved quite effective since a notable improvement of charge efficiency was observed at RT for the

ball-milled (BM)-γ' (≈ 90 % after the first cycle at C/10), allowing to reach nearly twice the capacity of γ'-carbo upon cycling (140 mAh g^{-1} after 50 cycles at C/10). Nevertheless, the charge/discharge profile of (BM)-γ' was modified, leading to a significant lowering of the working potential (2.8 V vs. 3.2 V for γ'-carbo). Hence, the implementation of a post-ball milling process did not allow a full improvement of the Na electrochemical properties of γ'-V_2O_5. Furthermore, this additional synthesis step is energy consuming and provides a limited control over particle size and shape (leading to the formation of defects and amorphization), and is also risky as it can generate excessive heating and undesirable phase transition of γ'-V_2O_5 into α-V_2O_5, as previously reported [19].

Differently, the wet chemistry route termed as "polyol process" was foreseen since the early 90's to be a versatile and promising method for the synthesis of finely divided metal and alloy powders [20]. More recently, this polyol process was successfully applied to synthesize a variety of pure sub-micrometer size vanadium oxides with well-defined shape and narrow size distribution, among them α-V_2O_5 [21]. Using such polyol synthesized- α-V_2O_5 as precursor should be a promising strategy to obtain γ-LiV_2O_5 and its delithiated form γ'-V_2O_5 with tailored morphology for improved Na insertion/deinsertion reactions.

In this work, we show that the polyol-based synthesis leading to homogeneous, fine and porous vanadium oxide precursor permits a clear improvement in the Na electrochemical insertion properties of the γ'-V_2O_5 polymorph. The obtained nanosized morphology allows to take benefit of the attractive Na insertion properties of γ'-V_2O_5, i. e. a significant available capacity of 145 mAh g^{-1}, a high working potential of about 3.25 V vs. Na^+/Na, an enhanced kinetics of sodium insertion/deinsertion, a high-rate capability and good cycle life. A detailed picture of the structural mechanism carried out by X-ray diffraction and Raman spectroscopy experiments shows highly reversible structural changes upon sodiation/desodiation as well as a particle size induced solid solution behavior. Finally, an electrochemical impedance spectroscopy study gives interesting insights on key kinetic parameters governing the Na insertion-extraction reaction in γ'-polyol and allowing a comprehensive understanding of its improved performance.

2. EXPERIMENTAL

2.1. Synthesis. γ-LiV_2O_5 was prepared by lithiation of a home-made α-V_2O_5 precursor according to the following procedure, which was reported to lead to very fine powder with a narrow particle size distribution [21]. Ammonium metavanadate powder NH_4VO_3 (Alfa Aesar, 99%) was slowly dissolved into ethylene glycol (Alfa Aesar 99%) at 110°C under continuous stirring. Once a yellow solution was formed, the temperature was increased to reach reflux conditions for 1 h. A vanadyl glycolate was then precipitated and washed with ethanol and dried at 80 °C. A thermal treatment at 450 °C in air for 2 h was performed in a box furnace to obtain the α-V_2O_5 powder. A key point of polyol α-V_2O_5 consists in obtaining a homogeneous grain size distribution with a particle size of ≈200 nm. Reaction of polyol α-V_2O_5 with an excess of lithium iodide in acetonitrile leads to the formation of the intermediate δ-LiV_2O_5 phase. After washing in acetonitrile and drying at 70°C, the obtained powder was heat treated at 300 °C for 2 hours under dynamic primary vacuum in a Büchi® furnace to allow the phase transition towards γ-LiV_2O_5. For comparison, we also prepared γ-LiV_2O_5 by carbothermal reduction method as detailed in [18], using commercial micrometric α-V_2O_5, carbon and lithium carbonate (Li_2CO_3) as precursors. The intimately mixed resulting powder was heat treated 2 hours at 600 °C under Ar atmosphere. To obtain the final γ'-V_2O_5 powder, a chemical oxidation of γ-LiV_2O_5 at RT was carried out in presence of an excess of nitronium tetrafluoroborate (NO_2BF_4) in acetonitrile under stirring. This step entails the complete removal of lithium ions from the interlayer structure of the γ phase, keeping the original puckered framework. The resulting γ'-V_2O_5 polymorphs prepared from carbothermal and polyol- synthesized γ-LiV_2O_5 will be referred as γ'-carbo and γ'-polyol, respectively.

2.2. Structural characterization. The morphology of the powders was investigated by using a field-emission scanning electron microscope (SEM) (Zeiss, Merlin-type) operating at 5 keV. The X-Ray Diffraction (XRD) experiments were performed using a PANalytical X-Pert Pro diffractometer equipped with a X'celerator linear detector and Co Kα source. Data were then processed on Eva software to identify peaks and adjust the cell parameters of the identified phases. The Raman spectra were measured with a LaBRAM HR 800 (Jobin-Yvon-Horiba) Raman micro-spectrometer including Edge filters and equipped for signal detection with a back illuminated charge coupled device detector (Spex CCD) cooled by Peltier effect to 200 K. A He:Ne laser (632.8 nm) was used as the excitation source. The spectra are measured in back-scattering geometry. The resolution is about 0.5 cm^{-1}. A long-distance 50X LWD objective was used to focus the laser light on sample surface to a spot size of 1 μm^2. To avoid

local heating of the sample, the power of the laser beam was adjusted to 0.2–0.5 mW with neutral filters of various optical densities. The structural study has been performed on electrochemically formed γ-$Na_xV_2O_5$ samples prepared at C/10 rate. After 2 hours of equilibrium time, the positive electrode was removed from the cell in an Ar-filled glove box, rinsed with DMC, and placed in appropriate airtight sample holders to be analyzed by X-ray diffraction and Raman spectroscopy. Raman spectra were recorded on 10 different spots of each electrode. Similar spectra were recovered for all the investigated points, whatever the Na uptake, indicating the good homogeneity of the electrodes.

2.3. Electrochemical tests. All the electrochemical measurements were performed with a VMP3 Biologic Multipotentiostat-Galvanostat apparatus. The electrolyte was a solution of 1 mol L^{-1} $NaClO_4$ in propylene carbonate (PC) containing fluoroethylene carbonate (FEC) as additive (2 Vol %). The positive electrode was made of a mixture of active material (γ'-V_2O_5 80 wt %), acetylene black (7.5 wt %), graphite (7.5 wt %) and teflon as binder agent (5 wt %) pressed on a stainless-steel grid under a pressure of 5 tons per cm^2. The mass loading was 5 $mg.cm^{-2}$.

Cycling experiments and galvanostatic intermittent titration technique (GITT) were carried out in two-electrode coin cells (CR 2032) with sodium disk as reference and auxiliary electrodes. The separator consisted of three glass Whatman microfiber filters and acted as an electrolyte tank. All the coin cells were assembled in the argon-filled glove box where water and oxygen concentrations are kept less than 1 ppm. The GITT measurement was programmed to supply a constant current of 14.7 mA g^{-1} for 30 min followed by an open circuit stand until the deviation dE/dt reaches values lower than 0.1 mV h^{-1}.

A conventional three-electrode cell filled with 1M $NaClO_4$ in PC was used in the glove box for impedance measurements. To ensure a reliable and stable reference potential all along the impedance acquisition, reference and counter electrodes were made of Li wires in separate compartments filled up with lithiated electrolyte during charge / discharge steps while a gold wire was used as counter electrode. Electrochemical Impedance Spectroscopy (EIS) spectra were measured on equilibrated working electrodes (S = 1 cm^2) as a function of x in γ-$Na_xV_2O_5$ in the 10^5 – 2.10^{-3} Hz range (excitation signal: 10 mV peak to peak). Impedance values are calculated for the lowest frequency of 2.10^{-3} Hz. Equilibrium was considered to be reached when the open circuit voltage remained stable (potential variations lower than 0.1 mV per hour) and the working electrode compositions

were adjusted by coulometric titration using a low current density corresponding to a C/20 rate (7.4 mA g^{-1}).

3. RESULTS AND DISCUSSION

3.1 Structural characterization. SEM images of the γ'-carbo and γ'-polyol powders are shown in **Figure 1**, with the same magnification. Quite different morphologies are observed: γ'-carbo exhibits aggregates with various sizes up to several hundred nanometers in thickness and several micrometers in plane. In contrast, γ'-polyol presents porous agglomerates composed of small grains with homogeneous size distribution in the 100 - 200 nm range. The present results show the great impact of the synthesis way on the grain shape, size and distribution and confirm the efficiency of the polyol process to obtain finely divided and homogeneous powder.

The X-ray diffraction pattern of γ'-polyol (**Fig. 2a**) exhibits the characteristics *hkl* reflections corresponding to an orthorhombic structure (JCPDS Card No. 01-085-2422, *Pnma* space group) with unit cell parameters a = 9.9484(2) Å, b = 3.5863(1) Å and c = 10.0459(3) Å in agreement with previous studies [12,16]. The Rietveld refinement of the XRD pattern (**Fig. S1**) confirms the presence of a pure and well-crystallized single phase. The structure of γ'-V_2O_5 (inset in **Fig. 2a**) retains the layered V_2O_5 framework although puckering of the layers is observed. Besides, the Raman spectrum (**Fig. 2b**) corresponds to the characteristic fingerprint of γ'-V_2O_5 composed of 21 peaks in the 90-1050 cm^{-1} wavenumber range. Based on the results of calculations, all the Raman peaks of γ'-V_2O_5 have been assigned to specific vibrational modes taking into account the structural data displayed in **Figure S2** [22–24]. The following vibrations of the chains can be identified: the stretching of the two shortest vanadyl bonds V_a-O_{1a} and V_b-O_{1b} at 1037, 1021 and 1003 cm^{-1}, the bond stretching vibrations localized within the V_a−O_3−V_b bridges at 752 and 603 cm^{-1}, and those of the V_a−O_{2a}−V_a and V_b−O_{2b}−V_b bridges forming the rails of the ladders at 722 and 694 cm^{-1}. Modes involving the V−O_2 ladder step (LS) bonds are observed at 532 and 500 cm^{-1}, while lower-frequency modes observed in the 90−400 cm^{-1} wavenumber range are related to the complex distortions of the ladders [22–24].

These whole structural and morphological characteristics show that the proposed polyol approach clearly allows mastering the particle size and distribution of γ′-V_2O_5 obtained as a pure, highly crystallized, finely divided and homogeneous powder. This synthesis way represents a clear benefit, not only compared to the carboreduction method but also versus the ball-milled process which was previously shown to generate defects, amorphization and

production of secondary phase due to undesirable and uncontrolled phase transition of γ′-V_2O_5 into α-V_2O_5 induced under excessive heating [10,19].

3.2 First charge-discharge properties. Figure 3 shows the first discharge-charge cycle at C/10 recorded for γ'-polyol, with that of γ'-carbo reported for comparison. Both materials show similar first discharge profile, i.e., one single step at c.a. 3.25 V vs. Na^+/Na involving the insertion of 1 Na^+ per mole of V_2O_5 (discharge capacity ≈ 147 mAh g^{-1}). However, the charge reaction is greatly improved in the case of γ'-polyol, as a result of the strong impact of the particle size and morphology. Indeed, unlike γ'-carbo for which a poor charge efficiency of 53% is observed, as previously reported[16], γ'-polyol exhibits a fully symmetric first discharge-charge cycle with a charge efficiency close to 100 % and a low hysteresis (about 100 mV). This remarkable result suggests highly reversible structural changes upon sodiation/desodiation.

In the case of γ'-carbo, the low efficiency of the first cycle indicates that a part of sodium ions remain trapped in the structure, as a result of a poor deinsertion kinetics [15,16]. This causal relationship was previously confirmed by the observed increase of the charge efficiency when the cycling experiments were carried out at higher temperature and at lower C rate (at 50°C, a nearly quantitative extraction of 97% Na ions was achieved at C/60) [16]. In addition, electrochemical impedance spectroscopy measurements revealed a huge increase in the electrode impedance during the first cycle which explained the important polarization at the end of the charge and the low efficiency of the first cycle [15]. Clearly, the high electrochemical reversibility achieved in the present case for γ '-polyol confirms the positive impact of a porous, fine and homogeneous morphology on the kinetics of the oxidation process.

3.3 Structural mechanism during the first discharge-charge cycle. In order to gain insight into the sodium insertion mechanism in γ'-polyol, we have investigated the structural answer upon electrochemical sodiation by performing *ex-situ* X-ray diffraction and Raman spectroscopy experiments during the first discharge-charge cycle in the 4.00 V- 1.75 V potential range.

The XRD patterns of discharged $Na_xV_2O_5$ electrodes in the $0 \leq x \leq 1$ composition range are gathered in **Figure 4**. The diffractogram of the pristine electrode (x = 0) is indexed using the P*nma* structure of γ'-V_2O_5. As soon as 0.1 Na is inserted in the γ'-V_2O_5 structure, a new set of peaks appears (highlighted in **Fig. 4a** by red vertical lines), with *hkl* reflections located at 2θ = 17.3, 20.3, 21.2, 27.4, 28.2, 32.0, 34.0, 35.4, 36.5, 37.0, 40.1, 45.6, 46.7, 47.7 and 48.0°.

This suggests the emergence of a new phase. It can be noted that for $0.1 \leq x \leq 0.4$, the intensities of these new peaks increase at the expense of those related to γ'-V_2O_5. This behavior is characteristic of a diphasic domain, the new phase growing at the expense of the pristine one, with the complete disappearance of γ'-V_2O_5 for x = 0.4. The $Na_{0.4}V_2O_5$ phase can be indexed like the fully discharged electrode $Na_{0.96}V_2O_5$, within the same P*nma* space group [16,17]. For $0 \leq x \leq 0.4$, the shifts of the *002* line towards lower angles (20.5° to 17.3°) and *200* peak towards higher angles (20.8° to 21.2°**)** in the diffractograms (see enlarged view in **Fig. 4b**) indicate an increase in the interlayer distance along the *c* axis, and a contraction along the *a* axis. The subsequent $Na_xV_2O_5$ patterns ($0.5 \leq x \leq 1$) do not exhibit new peaks but very slight shifts are observed for the *002* and *200* peaks, characteristics of a solid solution domain and indicating moderate expansion along the *c* axis and contraction along the *a* axis. The variations of cell parameters and volume of both phases during sodiation are gathered in **Figure 5**. The cell parameters of γ'-V_2O_5 (*a* = 9.94 Å, *b* = 3.58 Å, *c* = 10.04 Å) and $Na_xV_2O_5$ (*a* = 9.79 Å, *b* = 3.61 Å, *c* = 11.91 Å) are constant within the $0 \leq x \leq 0.4$ diphasic domain. Then, for x > 0.4, the *a* parameter decreases gradually (from 9.79 Å for x = 0.4 to 9.755 Å for x = 1) while *b* and *c* faintly increase (from *b* = 3.61 Å and *c* = 11.91 Å for x = 0.4 to *b* = 3.63 Å and *c* = 11.94 Å for x = 1). These almost linear evolutions confirm the existence of a solid solution domain for $0.4 < x \leq 1$. The volume expansion, of about 17 %, mainly takes place in the diphasic domain. It is indeed very remarkable that the electroformed γ-$Na_xV_2O_5$, ($x \geq 0.4$) bronze undergoes only tiny lattice parameters variations in the $0.4 \leq x \leq 1$ composition domain (less than 0.5%). This sodiated phase is characterized by a highly expanded interlayer *c* parameter (+1.9 Å between γ'-V_2O_5 and γ-NaV_2O_5) which probably allows insertion of Na ions for x > 0.4 without any further structural changes. It is worth also noticing the lowering of the *a* parameter in γ-$Na_xV_2O_5$ (-0.2 Å between γ-NaV_2O_5 and γ'-V_2O_5). This trend reveals an extra folding of the V_2O_5 sheets as a consequence of the shortening of the vanadium-vanadium distances upon reduction. Besides, at the end of the reduction process, the obtained lattice constants are in excellent agreement with those reported for electrochemically and chemically formed $Na_{0.96}V_2O_5$ [16,17]

The Raman spectra of the γ-$Na_xV_2O_5$ ($0 \leq x \leq 1$) electrodes recorded during the first discharge process are shown in **Figure 6.** Note that for each Na uptake, similar spectra were found for the 10 investigated points, which indicates the good homogeneity of the electrodes. Sodium insertion in γ'-polyol leads to the following spectral changes. For x = 0.1, five new bands are seen (indicated by red circles), located at 86, 473, 960, 990 and 1015 cm^{-1}, that coexist with

the Raman fingerprint of the pristine oxide (peaks indicated by black stars). For x = 0.25, the new bands are more intense and two additional peaks are observed at 110 and 323 cm^{-1}. For x = 0.4, the Raman spectrum is dominated by bands belonging to the new system while the presence of γ'-V_2O_5 is only revealed by small Raman features located at 92, 138, 170, 190 and 266 cm^{-1}. From x = 0.5 and up to the end of the discharge, the Raman signature of the single γ-$Na_xV_2O_5$ phase is observed, with bands at 86, 110, 155, 195, 216, 248, 295, 323, 389, 473, 546, 670, 715, 736, 960, 977 and 1004 cm^{-1}. This Raman fingerprint is also in excellent agreement with that previously reported for electrochemically and chemically formed $Na_{0.96}V_2O_5$ [16,17].

In summary, the evolution of the Raman spectra indicates the appearance of a new sodiated phase from x = 0.1 which coexists with the pristine γ'-V_2O_5 in the $0.1 \leq x \leq 0.4$ composition range and is pure in the $0.4 < x \leq 1$ domain. These findings are in line with the XRD study and confirm also that the sodiated γ-$Na_xV_2O_5$ phase does not undergo any structural variation at the atomic scale, as revealed by its invariant signature in the $0.4 < x \leq 1$ composition range.

This structural study during the discharge process points to the existence of a two-phase mechanism involved during sodium insertion in γ'-polyol. A sodiated phase is produced from the early Na content (x = 0.1) that coexists with γ'-V_2O_5 up to x = 0.4. Then a single-phase domain is observed in the $0.4 < x \leq 1$ composition range. Such mechanism exhibits in a first approach a strong similarity with that previously reported for γ'-carbo, characterized by a two-phase mechanism for $0 < x \leq 0.7$ followed by a narrow single phase region for $0.7 \leq x \leq 0.97$ [16]. However, in the present case, the much wider solid solution domain found for γ'-polyol V_2O_5 probably results from a downsizing effect, as previously reported in the case of Li insertion in anatase TiO_2 [25]. Such a finding should impact the electrochemical properties of γ'-polyol.

During the consecutive charge, both XRD and Raman spectroscopy indicate a reverse structural evolution (see **Figure 7 and S3**) and the complete recovery of the XRD and Raman spectrum of pristine γ'-V_2O_5 is observed at the end of a complete cycle. Hence, the first sodiation/desodiation cycle of γ'-polyol exhibits high electrochemical and structural reversibility. The restoration of the pristine material after one cycle indicates the sodiation/desodiation process concerns the whole electrode material in the case of γ'-polyol. This remarkable result probably comes from the specific morphology described above, promoting an homogeneous sodiation process and ionic transport and allowing the full

extraction of sodium, unlike what was observed in the case of γ'-carbo for which a sodiated phase γ-$Na_xV_2O_5$ ($0.5 \leq x \leq 0.97$) was still present after charging at RT.[16]

3.4 Kinetic study. In a first approach, the rate performance of γ'-polyol have been investigated by applying various current densities in the range C/10 –10 C. For each C rate, one typical cycle has been extracted and is reported in **Figure 8a**. Whatever the C rate, the shape of the discharge curves is maintained with a single voltage plateau located near 3.25 V vs. Na^+/Na and an excellent electrochemical reversibility. When the applied current increases from C/10 to 2 C, the capacity decreases by less than 30 %, from 145 to 103 mAh g^{-1}. In the same time, the hysteresis increases from 100 mV to ~ 320 mV, which represents lower values than those obtained with γ'-carbo (173 mV at C/10 and 664 mV at 1 C)[16]. These findings and the absence of huge polarization indicate the sodium ions diffusion is favored in the case of smaller active material particles and is not drastically impacted in this current range. For higher 5C rate, the gravimetric capacity decreases while hysteresis increases (70 mAh g^{-1} – 600 mV). Whatever the C rate, for all cycles, recovered discharge and charge capacities are reported as a function of cycle number in **Figure 8b**. Capacities higher than 100 mAh g^{-1} for C rates increasing from C/10 until 2 C with an excellent 100 % coulombic efficiency are confirmed. For 5C rate, lower capacities about 70 mAh g^{-1} is achieved and a coulombic efficiencies < 100 % is observed due to a high polarization. However, the subsequent imposition of a lower current density of C/10 leads to the recovery of the initial discharge capacity, showing the material has not been impacted by the application of high C rates.

The attractive rate capability performance exhibited by γ'-polyol have prompted us to investigate the kinetics parameters of the electrochemical sodium process during the first reduction. Typical impedance spectra of γ-$Na_xV_2O_5$ ($0 \leq x < 1$) electrodes are reported in **Figure 9**. Clearly, these impedance diagrams are strongly dependent of the sodium uptake. The pristine electrode exhibits a high impedance value (|Z| = 936 Ω), largely higher than for any sodiated one. As soon as a few sodium ions (x = 0.02) are inserted in the material, a huge decrease of impedance is observed, to reach ~ 180 Ω. Then |Z| slightly decreases up to 60 Ω for x = 0.2 before increasing to 185 Ω for x = 0.8. The overpotential observed at the very first beginning of the discharge (Fig. 3) and then decreasing with sodiation can be related to this peculiar impedance evolution with x.

The present moderate impedance variation upon sodiation (100-200 Ω) compared to the higher variations observed for γ'-carbo (100-700 Ω) [15] might indicate a better accommodation of the volume change (17 %, see **Fig. 5d**) allowed by the lower particle size of γ'-polyol. In the present case, the loss of inter-particles contact is probably minimized.

Whatever the x value, the impedance spectra (**Fig. 9**) present a similar shape: two depressed semi-circles at high and medium frequencies, with characteristic frequencies of about $f_1 \approx 1000–1500$ Hz and $f_2 \approx 50–100$ Hz, respectively. The semi-circle at high frequency, practically unchanged with x, is directly followed by a second semi-circle whose size is x dependent. This latter can be then safely ascribed to the charge transfer. At low frequencies, a straight line with a phase angle of 45° is observed (**Fig. 10a**), which corresponds to the Warburg region (when $\omega >> 2D_{Na}/L^2$, D_{Na} and L being respectively the apparent chemical diffusion coefficient of sodium and the maximum length of the diffusion pathway). This Warburg region is followed in some cases by a quasi-vertical line (when $\omega << 2D_{Na}/L^2$) at low frequency.

All the spectra can be fitted with the equivalent electrical circuit presented in inset of **Figure 9b** [26]. As expected with the three-electrode cell and such an electrolyte, the value of the electrolyte resistance R_0 is low and stable, around 2 Ω. The characteristic frequency f_1 (i.e., the frequency at which the top of the first semicircle is reached) and the resistance R_1 (i.e., the diameter of the first fitted semi-circle) keep nearly the same values in the whole composition range, i.e., 1.10^3–$1.5.10^3$ Hz and 3.3 Ω, respectively. This first x independent semi-circle can be attributed to the presence of a stable film on the current collector.

The second semi-circle observed at f_2 characteristic frequency is x dependent and can be ascribed to charge transfer. An increase of the charge transfer resistance, R_2, is observed with the sodium content, from 10 Ω to 28 Ω (**Figs. 9b** and **10b**) while at the same time, f_2 slightly decreases from 100 Hz for x = 0.02 to 46 Hz for x = 0.8**.** In fact, the charge transfer resistance slightly increases between x = 0.02 and 0.4 when γ'-V_2O_5 and γ-$Na_{\sim 0.4}V_2O_5$ coexist, and then a little more significantly in the monophasic $0.4 \leq x \leq 0.8$ region **(Fig. 10b)**. This slowdown in charge transfer kinetics can be related to the localized character of electrons in the fully sodiated phase [17]. The resulting double layer capacity (C_{DL} = CPE_2 here) is kept quite constant (~170 µF cm^{-2}) for $x \leq 0.4$ and decreases by 25%, to reach 128 µF cm^{-2} for x = 0.8. These high C_{DL} values reveal an electrochemical surface area for γ'-polyol significantly higher than that offered by γ'-carbo [15], by a factor ≈ 4-5 and even twice that reported for the ball-milled

powder (90 µF cm^{-2})[19], which promotes an homogeneous insertion and extraction of sodium ions.

From the Warburg domain present in all the spectra (**Fig. 10a**), the apparent Na chemical diffusion coefficient D_{Na} has been calculated according to **equation (1)**:

$$D_{Na} = \left(\frac{V_m}{\sqrt{2}nFS}\left(\frac{dE}{dx}\right)_x \frac{1}{A_w}\right)^2 \qquad \textbf{eq(1)}$$

A_w is the Warburg prefactor (which was calculated for each x value, based on the linear relation between $\left(\frac{1}{\sqrt{\omega}}\right)_x$ and Re(Z), see **Fig. 11a**), V_m is the molar volume of the compound (V_m = 53.91 cm^3 for γ'-V_2O_5 and V_m = 63.62 cm^3 for γ-$Na_xV_2O_5$ (0.4 ≤ x) – a linear variation of the volume is considered in the sodium content varying from 0 to 0.4), n the electron number in the considered redox reaction (n = 1), F the Faraday's constant (F = 96500 C mol^{-1}), S is the geometric surface area of the electrode (1 cm^2), $\left(\frac{dE}{dx}\right)_x$ the slope, at fixed x, of the equilibrium potential composition curve.

On the other hand, the galvanostatic intermittent titration technique (GITT) has been carried out and the different values of D_{Na} have been calculated according to **equation (2)**:

$$D_{Na} = \frac{4}{\pi\tau}\left(\frac{m_B V_m}{M_B S}\right)^2 \left(\frac{\Delta Es}{\Delta Et}\right)^2 \qquad \textbf{eq(2)}$$

The GITT relaxation curve is shown in **Figure S4**. In **equation (2)**, τ is the duration during which the current is applied (30 mn), m_B is the active material mass in the electrode, M_B is the molar weight of V_2O_5, ΔEs is the difference between the equilibrium potential reached at the end of the relaxation scheduled after the galvanostatic step and the one obtained at the end of the previous relaxation (measured when dE/dt < 0.1 mV h^{-1}), ΔEt is the potential variation registered during the galvanostatic step after ohmic drop subtraction.

As shown in **Figure 11b**, values of D_{Na} obtained from EIS and GITT measurements are of the same order of magnitude, increasing from 3.10^{-13} to 10^{-9} cm^2 s^{-1} with x. In the sodium content range corresponding to the biphasic domain (x ≤ 0.4), the apparent chemical diffusion coefficient is roughly constant, around 10^{-12} cm^2 s^{-1} while it significantly increases up to 10^{-9} cm^2 s^{-1} in the monophasic region. It is worth noting that the kinetics of sodium transport is faster in the solid solution domain (x > 0.4) than in the diphasic region (x < 0.4). This finding is in line with the good rate capability observed in **Figure 8.** Previous works on Li diffusion

in $LiFePO_4$ also reported an apparent chemical Li diffusion coefficient much higher by several orders of magnitude in the Li rich single phase than in biphasic region [27–29]. The orders of magnitude found for D_{Na} in γ'-V_2O_5 values are in satisfactory agreement with data from literature in the case of sodiated oxides like $Na_{0.33}V_2O_5$ [30,31], Na_xCoO_2 [32] and P2-$Na_{0.67}MnO_2$ [33].

3.5 Cycling performance. Cycling performance of γ'-polyol has been examined for an applied current density of 147 mA g^{-1} (1 C rate). Some of the first two hundred cycles are presented in **Figure 12**. The evolution of the specific capacity as a function of cycle number is presented in inset. A slight decrease is observed after 200 cycles, from 126 mAh g^{-1} to 115 mAh g^{-1} (9%) while galvanostatic cycles retain the same shape, without increased hysteresis. The electrochemical performances obtained with the γ'-polyol polymorph differ from those presented in the literature on different aspects. First, most of the studies on the Na^+ / V_2O_5 system presents a working voltage between 2**.7** V and 1.9 V [9,34,35] while it reaches a significantly higher value of 3.25 V in the case of γ'-polyol. Second, the achieved capacities are often less than 200 mAh g^{-1}, although the range of potential scanned is wider: for example D. Su *et al* obtain from 110 mAh g^{-1} to 150 mAh g^{-1}, respectively with V_2O_5 hollow nanospheres and bilayered V_2O_5 nanobelts, after 100 cycles between 4 and 1 V at 160 mA g^{-1} [9,34] while sponge-like V_2O_5 xerogel prepared by K. Zhu *et al* exhibit a capacity of only ~ 90 mAh g^{-1} after 100 cycles between 4 and 1.25 V at 100 mA g^{-1} [35]. A more recent study reports a limited capacity of 78 mAh g^{-1} at the 100th cycle for V_2O_5 single-crystalline nanowires cycled between 4 and 1 V at 100 mA g^{-1} (0.6 C) [36]. Finally, considering capacities reached by these different kinds of nanomaterials (nanospheres, nanobelts, nanosheets, nanowires), during the sodiation step at a potential of 1.75 V, value which corresponds to the lower limit in the present study, and the working potential discussed above, specific energy densities delivered by those systems remain lower than the 400 Wh kg^{-1} afforded by the present Na^+ / γ'-polyol V_2O_5 system. This characteristic constitutes an undeniable asset for the γ' polymorph prepared according to this solution synthesis route.

4. CONCLUSION

In this work, we report the Na electrochemical features of γ'-V_2O_5 polymorph synthesized via a solution technique, using polyol synthesized- α-V_2O_5 as precursor. We show that this synthesis route allows to get the γ'-V_2O_5 polymorph with tailored morphology, i.e., made of nanoparticles 100-200 nm long against big platelets of a few microns for γ'-carbo made from a solid-state reaction. The obtained polyol-γ'-V_2O_5 cathode material exhibited an appealing discharge capacity of 145 mAh g^{-1} available at a high potential 3.25 V vs Na^+/Na, and a quantitative charge process, allowing to overcome the huge drawback of low charge efficiency exhibited by γ'-carbo and limiting the effective capacity to only half this value, i.e., 70 mAh g^{-1}. Enhanced electrochemical performance for polyol-γ'-V_2O_5 are also highlighted in terms of rate capability allowing to benefit from a capacity of 100 mAh g^{-1} at 2 C. The structural results presented in this work show that crystal particle size has also a striking impact on the Na-insertion/extraction behavior: the nanosizing approach promotes the solubility and solid solution behavior. Indeed, compared to the results previously reported for γ'-carbo, Na insertion in polyol-γ'-V_2O_5 occurs through a significantly shortened diphasic region ($0 < x \leq 0.4$ against $0 < x \leq 0.7$) while the solid solution γ-$Na_xV_2O_5$ domain is expanded ($0.4 < x \leq 1$ against $0.7 < x \leq 1$). Impedance spectroscopy study reveal a moderate change in electrode impedance upon sodiation and a low decrease of charge transfer kinetics. A significant C_{DL} increase by a factor 4-5 vs microsized polymorph illustrates the significant nanosize effect on the electrochemical surface enhancement. The evolution of the chemical diffusion coefficient D_{Na} shows a faster diffusion in the single-phase region than in the diphasic domain. The present work shows that optimized electrochemical properties achieved with the use of polyol synthesis makes the γ'-V_2O_5 polymorph a competitive cathode material for NIB combining a high operating voltage of 3.25 V vs Na^+/Na, a high capacity of 140 mAh g^{-1}, a high-rate capability, excellent charge efficiency and good cycle life.

5- ACKNOWLEDGMENTS

One of the authors DB wishes to thank the Ministry of Education and Science of Kazakhstan (grant number AP05136016-ZRABS), French Embassy in Astana, Kazakhstan and Campus France for financial support.

REFERENCES

(1) Larcher, D.; Tarascon, J.-M. Towards Greener and More Sustainable Batteries for Electrical Energy Storage. *Nature Chem* **2015**, *7* (1), 19–29. https://doi.org/10.1038/nchem.2085.

(2) Li, F.; Wei, Z.; Manthiram, A.; Feng, Y.; Ma, J.; Mai, L. Sodium-Based Batteries: From Critical Materials to Battery Systems. *J. Mater. Chem. A* **2019**, *7* (16), 9406–9431. https://doi.org/10.1039/C8TA11999F.

(3) Yabuuchi, N.; Kubota, K.; Dahbi, M.; Komaba, S. Research Development on Sodium-Ion Batteries. *Chem. Rev.* **2014**, *114* (23), 11636–11682. https://doi.org/10.1021/cr500192f.

(4) Sodium-Ion Battery Market. https://straitsresearch.com/report/sodium-ion-battery-market.

(5) Yao, J.; Li, Y.; Massé, R. C.; Uchaker, E.; Cao, G. Revitalized Interest in Vanadium Pentoxide as Cathode Material for Lithium-Ion Batteries and Beyond. *Energy Storage Mater.* **2018**, *11*, 205–259. https://doi.org/10.1016/j.ensm.2017.10.014.

(6) West, K. Sodium Insertion in Vanadium Oxides. *Solid State Ionics* **1988**, *28–30*, 1128–1131. https://doi.org/10.1016/0167-2738(88)90343-8.

(7) Pereira- Ramos, J. P.; Messina, R.; Perichon, J. Electrochemical Formation of Vanadium Pentoxide Bronzes $M_xV_2O_5$ in Molten Dimethylsulfone. *J. Electrochem. Soc.* **1988**, *135* (12), 3050–3057. https://doi.org/10.1149/1.2095486.

(8) Muller-Bouvet, D.; Baddour-Hadjean, R.; Tanabe, M.; Huynh, L. T. N.; Le, M. L. P.; Pereira-Ramos, J. P. Electrochemically Formed α'-NaV_2O_5: A New Sodium Intercalation Compound. *Electrochim. Acta* **2015**, *176*, 586–593. https://doi.org/10.1016/j.electacta.2015.07.030.

(9) Su, D. W.; Dou, S. X.; Wang, G. X. Hierarchical Orthorhombic V2O5 Hollow Nanospheres as High Performance Cathode Materials for Sodium-Ion Batteries. *J. Mater. Chem. A* **2014**, *2* (29), 11185. https://doi.org/10.1039/c4ta01751j.

(10) Baddour-Hadjean, R.; Safrany Renard, M.; Emery, N.; Huynh, L. T. N.; Le, M. L. P.; Pereira-Ramos, J. P. The Richness of V_2O_5 Polymorphs as Superior Cathode Materials for Sodium Insertion. *Electrochim. Acta* **2018**, *270*, 129–137. https://doi.org/10.1016/j.electacta.2018.03.062.

(11) Tepavcevic, S.; Xiong, H.; Stamenkovic, V. R.; Zuo, X.; Balasubramanian, M.; Prakapenka, V. B.; Johnson, C. S.; Rajh, T. Nanostructured Bilayered Vanadium Oxide Electrodes for Rechargeable Sodium-Ion Batteries. *ACS Nano* **2012**, *6* (1), 530–538. https://doi.org/10.1021/nn203869a.

(12) Cocciantelli, J. M.; Gravereau, P.; Doumerc, J. P.; Pouchard, M.; Hagenmuller, P. On the Preparation and Characterization of a New Polymorph of V_2O_5. *J. Solid State Chem.* **1991**, *93* (2), 497–502. https://doi.org/10.1016/0022-4596(91)90323-A.

(13) Baddour-Hadjean, R.; Renard, M. S.; Pereira-Ramos, J. P. Kinetic Insight into the Electrochemical Lithium Insertion Process in the Puckered-Layer γ'-V_2O_5 Polymorph. *J. Electrochem. Soc.* **2019**, *166* (14), A3474–A3479. https://doi.org/10.1149/2.1211914jes.

(14) Baddour-Hadjean, R.; Safrany Renard, M.; Pereira-Ramos, J. P. Unraveling the Structural Mechanism of Li Insertion in γ′-V_2O_5 and Its Effect on Cycling Properties. *Acta Mater.* **2019**, *165*, 183–191. https://doi.org/10.1016/j.actamat.2018.11.043.

(15) Safrany Renard, M.; Baddour-Hadjean, R.; Pereira-Ramos, J. P. Kinetic Insight into the Electrochemical Sodium Insertion-Extraction Mechanism of the Puckered γ′-V_2O_5 Polymorph. *Electrochim. Acta* **2019**, *322*, 134670. https://doi.org/10.1016/j.electacta.2019.134670.

(16) Safrany Renard, M.; Emery, N.; Baddour-Hadjean, R.; Pereira-Ramos, J.-P. γ'-V_2O_5: A New High Voltage Cathode Material for Sodium-Ion Battery. *Electrochim. Acta* **2017**, *252*, 4–11. https://doi.org/10.1016/j.electacta.2017.08.175.
(17) Emery, N.; Baddour-Hadjean, R.; Batyrbekuly, D.; Laïk, B.; Bakenov, Z.; Pereira-Ramos, J.-P. γ-$Na_{0.96}V_2O_5$: A New Competitive Cathode Material for Sodium-Ion Batteries Synthesized by a Soft Chemistry Route. *Chem. Mater.* **2018**, *30* (15), 5305–5314. https://doi.org/10.1021/acs.chemmater.8b02066.
(18) Barker, J.; Saidi, M. Y.; Swoyer, J. L. Performance Evaluation of the Electroactive Material, γ-LiV_2O_5 Made by a Carbothermal Reduction Method. *J. Electrochem. Soc.* **2003**, *150* (9), A1267. https://doi.org/10.1149/1.1600462.
(19) Baddour-Hadjean, R.; Safrany Renard, M.; Pereira-Ramos, J.-P. Enhanced Electrochemical Properties of Ball-Milled γ′-V_2O_5 as Cathode Material for Na-Ion Batteries: A Structural and Kinetic Investigation. *J. Power Sources* **2021**, *482*, 229017. https://doi.org/10.1016/j.jpowsour.2020.229017.
(20) Fievet, F.; Fievet-Vincent, F.; Lagier, J.-P.; Dumont, B.; Figlarz, M. Controlled Nucleation and Growth of Micrometre-Size Copper Particles Prepared by the Polyol Process. *J. Mater. Chem.* **1993**, *3* (6), 627. https://doi.org/10.1039/jm9930300627.
(21) Mjejri, I.; Rougier, A.; Gaudon, M. Low-Cost and Facile Synthesis of the Vanadium Oxides V_2O_3, VO_2 and V_2O_5 and Their Magnetic, Thermochromic and Electrochromic Properties. *Inorg. Chem.* **2017**, *56* (3), 1734–1741. https://doi.org/10.1021/acs.inorgchem.6b02880.
(22) Smirnov, M. B.; Roginskii, E. M.; Smirnov, K. S.; Baddour-Hadjean, R.; Pereira-Ramos, J.-P. Unraveling the Structure–Raman Spectra Relationships in V_2O_5 Polymorphs via a Comprehensive Experimental and DFT Study. *Inorg. Chem.* **2018**, *57* (15), 9190–9204. https://doi.org/10.1021/acs.inorgchem.8b01212.
(23) Baddour-Hadjean, R.; Smirnov, M. B.; Kazimirov, V. Y.; Smirnov, K. S.; Pereira-Ramos, J.-P. The Raman Spectrum of the γ′-V_2O_5 Polymorph: A Combined Experimental and DFT Study. *J. Raman Spectrosc.* **2015**, *46* (4), 406–412. https://doi.org/10.1002/jrs.4660.
(24) Roginskii, E. M.; Smirnov, M. B.; Smirnov, K. S.; Baddour-Hadjean, R.; Pereira-Ramos, J.-P.; Smirnov, A. N.; Davydov, V. Yu. A Computational and Spectroscopic Study of the Electronic Structure of V_2O_5 -Based Cathode Materials. *J. Phys. Chem. C* **2021**, *125* (10), 5848–5858. https://doi.org/10.1021/acs.jpcc.0c11285.
(25) Wagemaker, M.; Borghols, W. J. H.; Mulder, F. M. Large Impact of Particle Size on Insertion Reactions. A Case for Anatase Li_xTiO_2. *J. Am. Chem. Soc.* **2007**, *129* (14), 4323–4327. https://doi.org/10.1021/ja067733p.
(26) Ho, C.; Raistrick, I. D.; Huggins, R. A. Application of A- C Techniques to the Study of Lithium Diffusion in Tungsten Trioxide Thin Films. *J. Electrochem. Soc.* **1980**, *127* (2), 343–350. https://doi.org/10.1149/1.2129668.
(27) Li, D.; Zhang, T.; Liu, X.; He, P.; Peng, R.; Wang, M.; Han, M.; Zhou, H. A Hybrid Phase-Transition Model of Olivine $LiFePO_4$ for the Charge and Discharge Processes. *J. Power Sources* **2013**, *233*, 299–303. https://doi.org/10.1016/j.jpowsour.2013.01.133.
(28) Gao, C.; Zhou, J.; Liu, G.; Wang, L. Lithium-Ions Diffusion Kinetic in $LiFePO_4$/Carbon Nanoparticles Synthesized by Microwave Plasma Chemical Vapor Deposition for Lithium-Ion Batteries. *Appl. Surf. Sci.* **2018**, *433*, 35–44. https://doi.org/10.1016/j.apsusc.2017.10.034.
(29) Milev, A.; George, L.; Khan, S.; Selvam, P.; Kamali Kannangara, G. S. Li-Ion Kinetics in LiFePO4 /Carbon Nanocomposite Prepared by a Two-Step Process: The Role of Phase Composition. *Electrochim. Acta* **2016**, *209*, 565–573. https://doi.org/10.1016/j.electacta.2016.05.097.

(30) Bach, S.; Baffier, N.; Pereiraramos, J.; Messina, R. Electrochemical Sodium Intercalation in Na0.33V2O5 Bronze Synthesized by a Sol-Gel Process. *Solid State Ionics* **1989**, *37* (1), 41–49. https://doi.org/10.1016/0167-2738(89)90285-3.
(31) Jiang, D.; Wang, H.; Li, G.; Li, G.; Lan, X.; Abib, M. H.; Zhang, Z.; Jiang, Y. Self-Combustion Synthesis and Ion Diffusion Performance of NaV_6O_{15} Nanoplates as Cathode Materials for Sodium-Ion Batteries. *J. Electrochem. Soc.* **2015**, *162* (4), A697–A703. https://doi.org/10.1149/2.0701504jes.
(32) Rami Reddy, B. V.; Ravikumar, R.; Nithya, C.; Gopukumar, S. High Performance $Na_x CoO_2$ as a Cathode Material for Rechargeable Sodium Batteries. *J. Mater. Chem. A* **2015**, *3* (35), 18059–18063. https://doi.org/10.1039/C5TA03173G.
(33) Tie, D.; Gao, G.; Xia, F.; Yue, R.; Wang, Q.; Qi, R.; Wang, B.; Zhao, Y. Modulating the Interlayer Spacing and Na^+ /Vacancy Disordering of P2-$Na_{0.67}MnO_2$ for Fast Diffusion and High-Rate Sodium Storage. *ACS Appl. Mater. Interfaces* **2019**, *11* (7), 6978–6985. https://doi.org/10.1021/acsami.8b19134.
(34) Su, D.; Wang, G. Single-Crystalline Bilayered V_2O_5 Nanobelts for High-Capacity Sodium-Ion Batteries. *ACS Nano* **2013**, *7* (12), 11218–11226. https://doi.org/10.1021/nn405014d.
(35) Zhu, K.; Zhang, C.; Guo, S.; Yu, H.; Liao, K.; Chen, G.; Wei, Y.; Zhou, H. Sponge- Like Cathode Material Self- Assembled from Two- Dimensional V_2O_5 Nanosheets for Sodium- Ion Batteries. *ChemElectroChem* **2015**, *2* (11), 1660–1664. https://doi.org/10.1002/celc.201500240.
(36) Li, Y.; Ji, J.; Yao, J.; Zhang, Y.; Huang, B.; Cao, G. Sodium Ion Storage Performance and Mechanism in Orthorhombic V_2O_5 Single-Crystalline Nanowires. *Sci. China Mater.* **2021**, *64* (3), 557–570. https://doi.org/10.1007/s40843-020-1468-6.

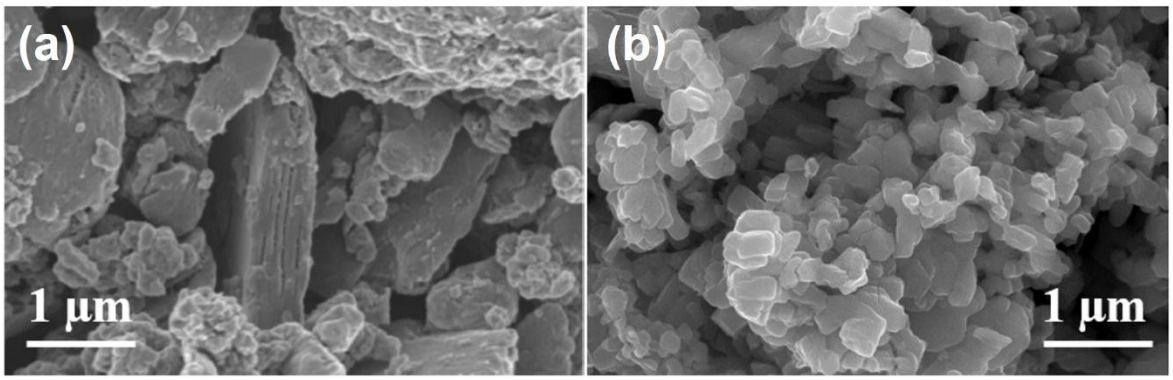

Figure 1. SEM images of γ'-carbo (a) and γ'-polyol (b)

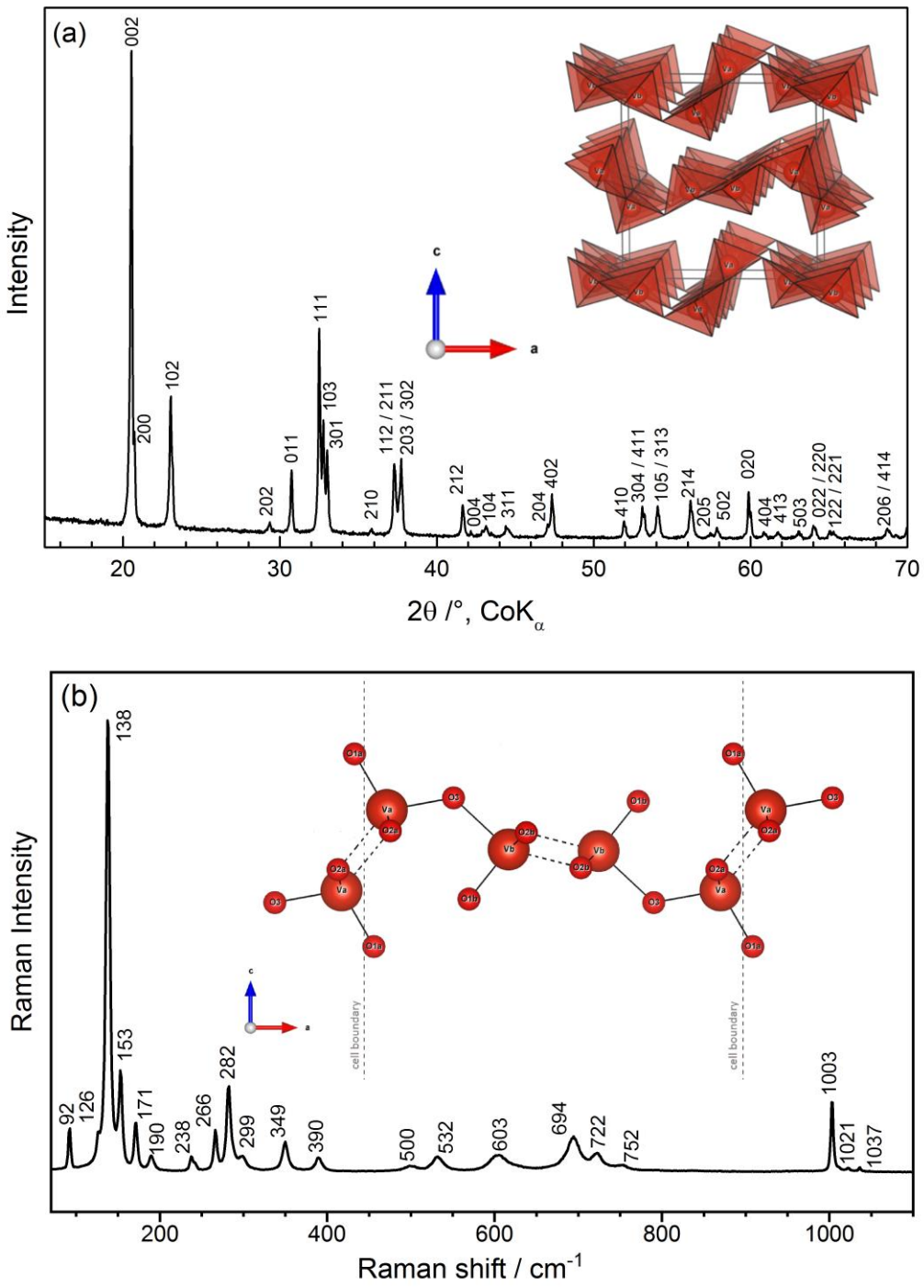

Figure 2. X-ray diffractogram (a) and Raman spectrum (b) of γ'-polyol V_2O_5. In inset: crystal structure and its projection along the *b*-crystallographic direction.

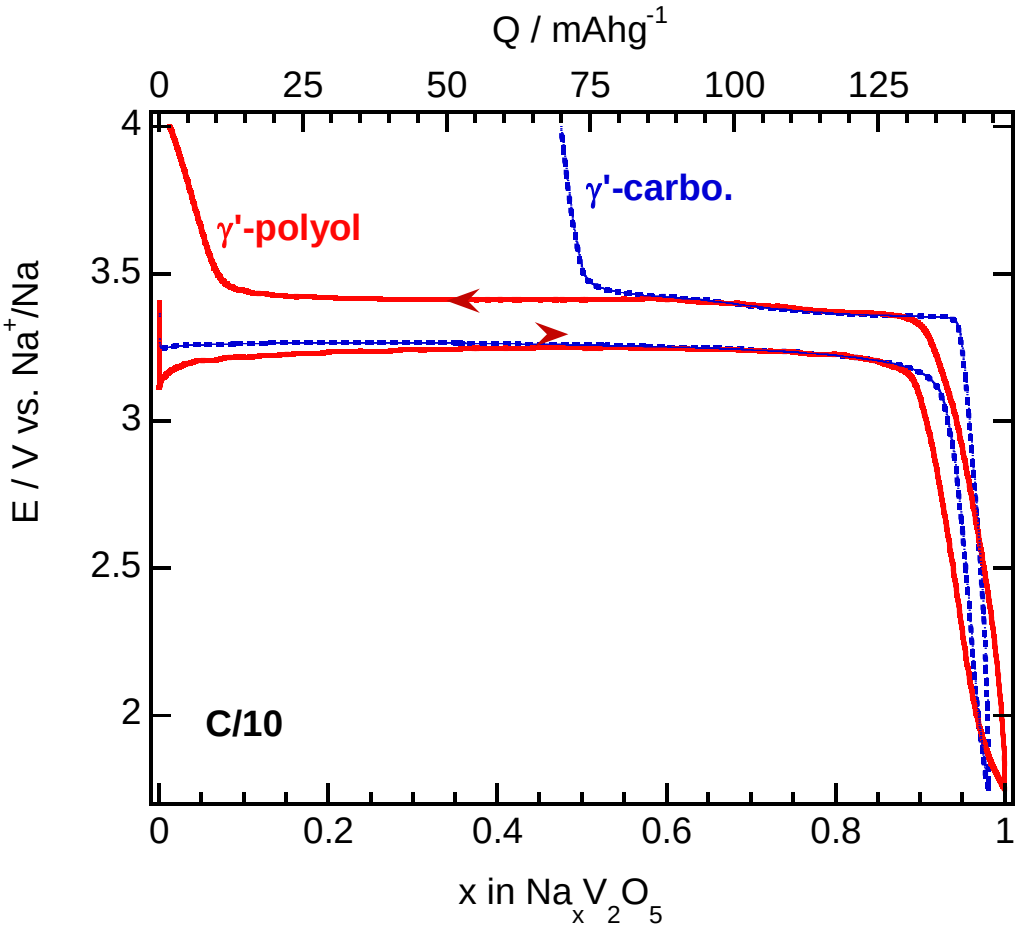

Figure 3. First discharge/charge cycle of γ'-polyol (red plain line) and γ'-carbo (blue dashed line) at C/10 in 1 mol L^{-1} $NaClO_4$-PC-2 vol. % FEC in the 4.0V – 1.75 V potential range.

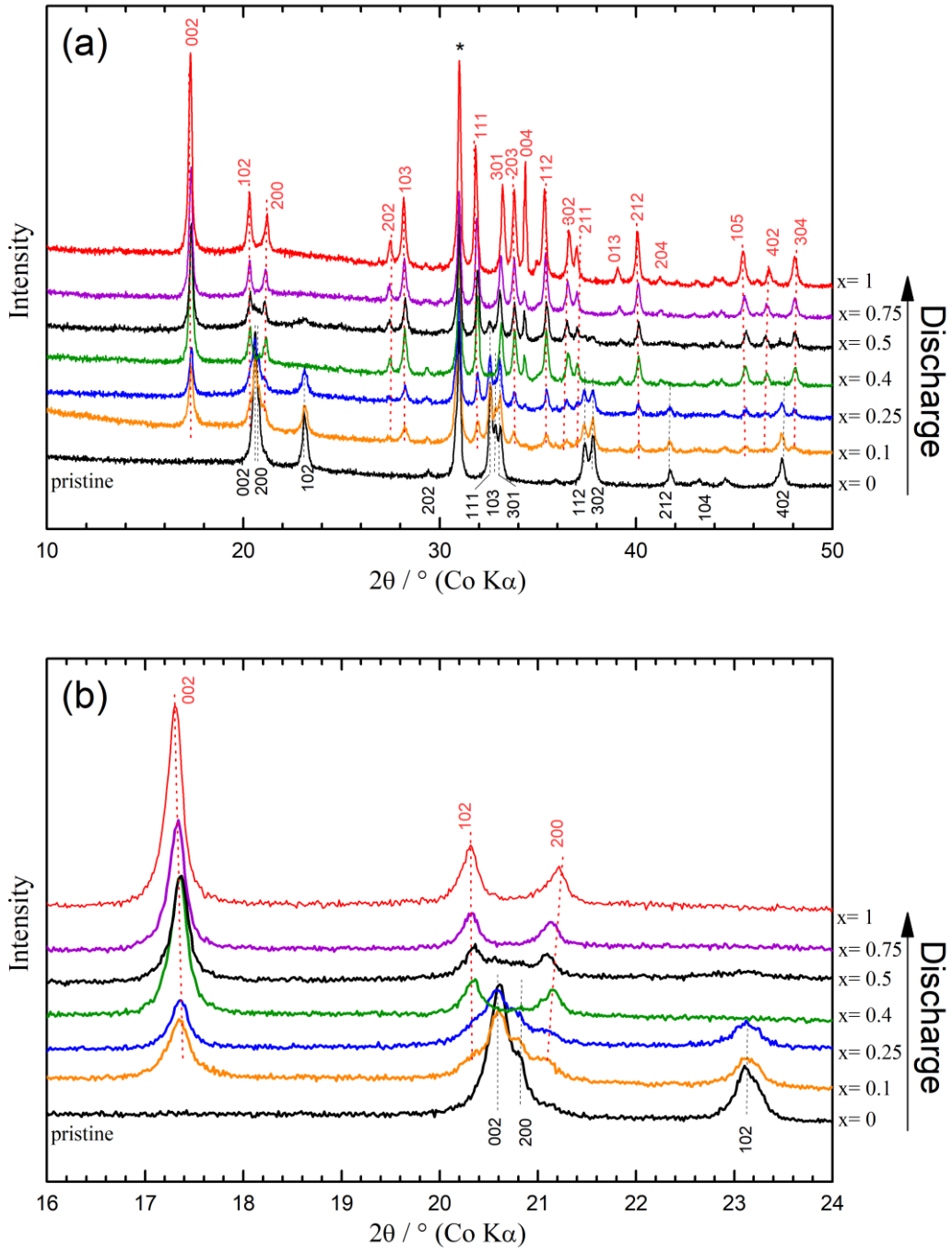

Figure 4. XRD patterns in the 10-50° (a) and 16-24° (b) 2θ regions of discharged $Na_xV_2O_5$ electrodes in the $0 \leq x \leq 1$ composition range. Lower indexation (in black) is related to γ'-V_2O_5 while the upper one (in red) corresponds to that of γ-$Na_xV_2O_5$. * : graphite reflection

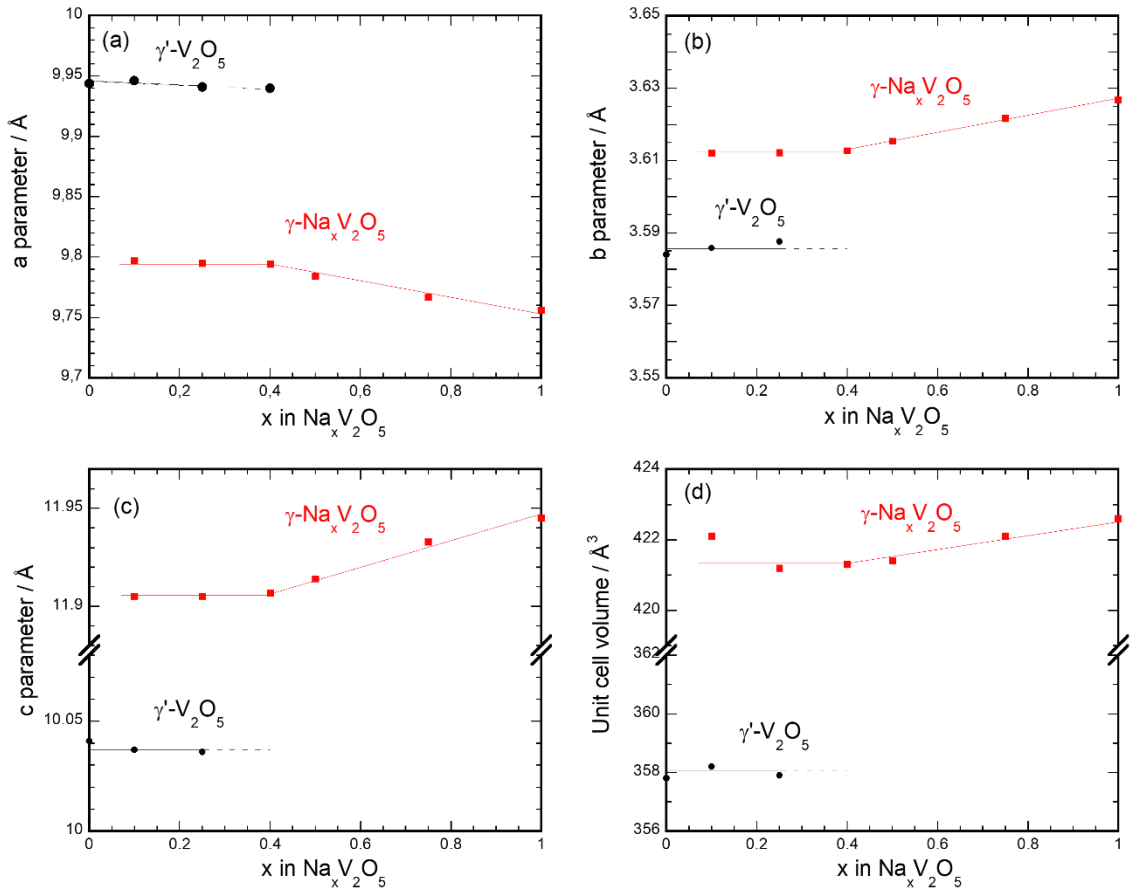

Figure 5. Evolution of the cell parameters and unit cell volume of the identified phases (• and ■ respectively for γ'-V_2O_5 and γ-$Na_xV_2O_5$) during the first discharge of γ'-polyol.

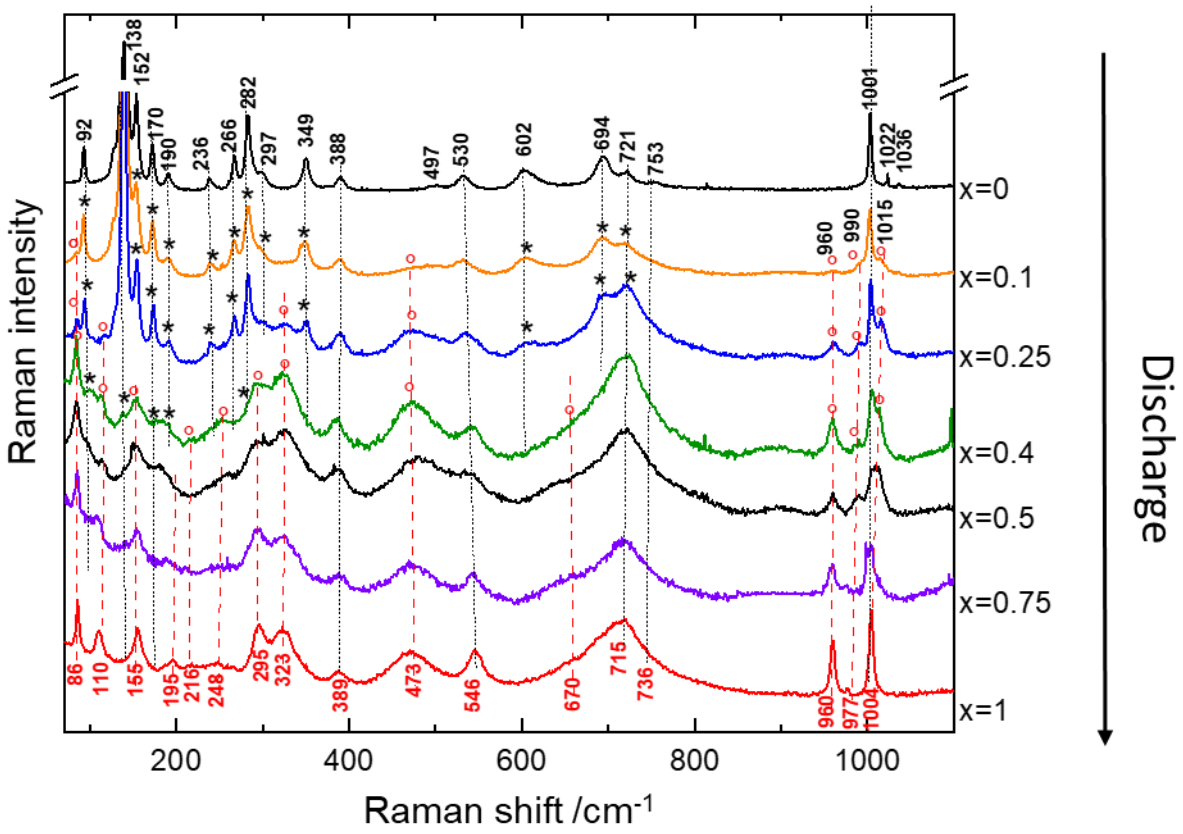

Figure 6. Raman spectra of discharged γ–$Na_xV_2O_5$ electrodes in the $0 \leq x \leq 1$ composition range. *: Raman bands of γ'-V_2O_5; °: Raman bands of the sodiated phase

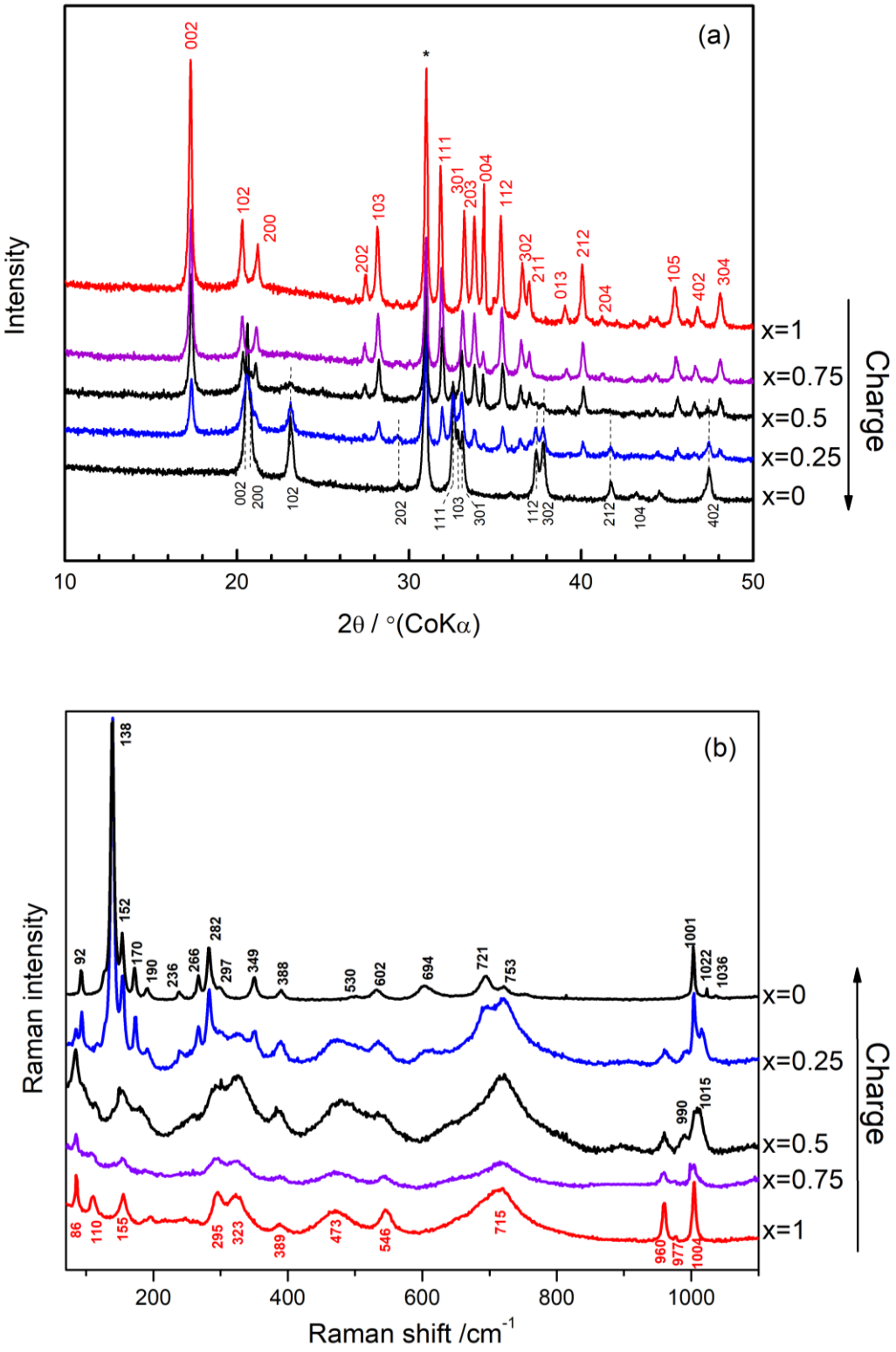

Figure 7. XRD (a) and Raman spectra (b) of charged γ-$Na_xV_2O_5$ electrodes in the $0 \leq x \leq 1$ composition range.

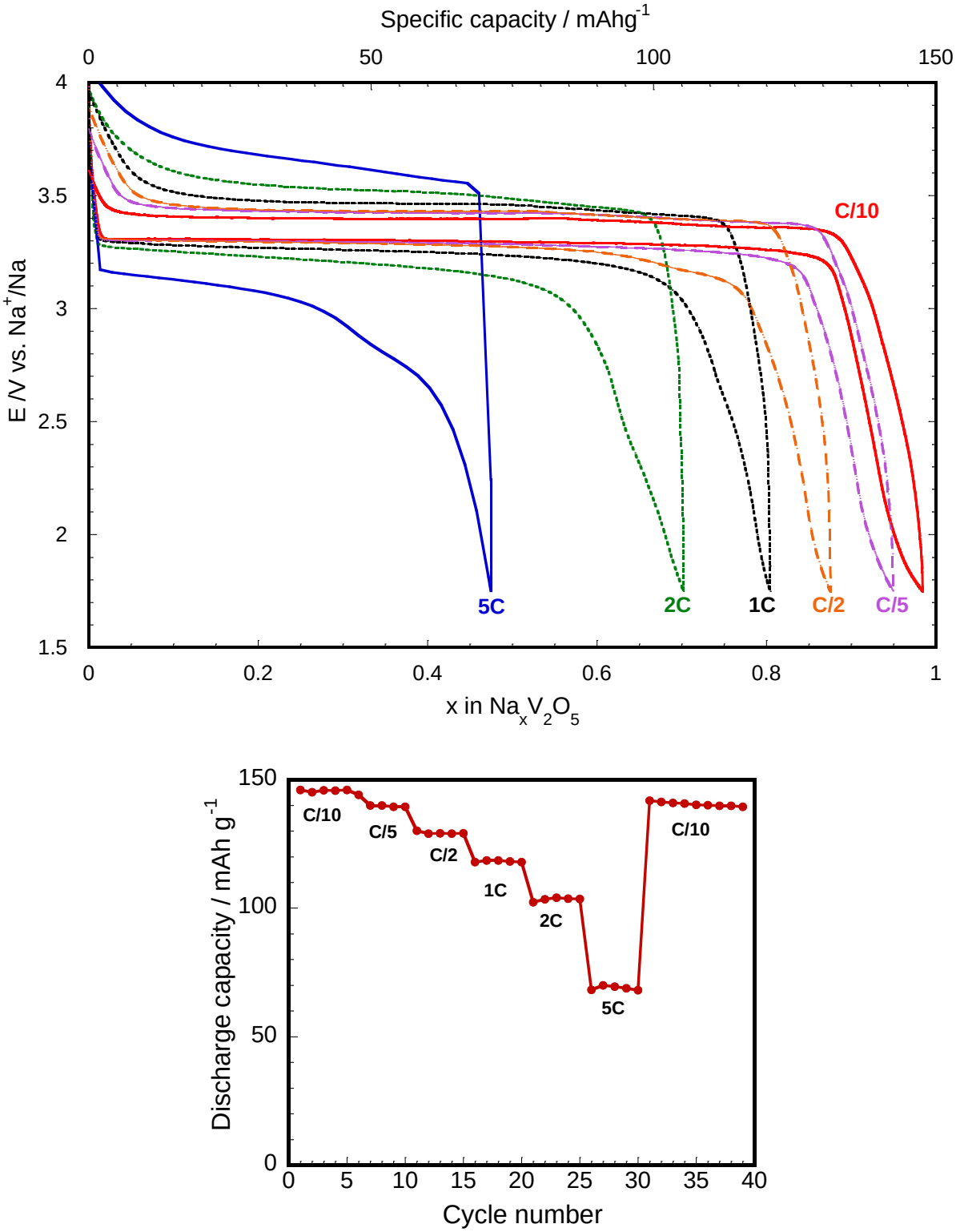

Figure 8. Rate capability study of γ'-V_2O_5 polyol in 1 mol L^{-1} $NaClO_4$-PC-2 vol. % FEC in the 4 V – 1.75 V potential range. (a) Typical galvanostatic cycles as a function of C rate (b) Evolution of the specific capacity upon cycling at different C rates.

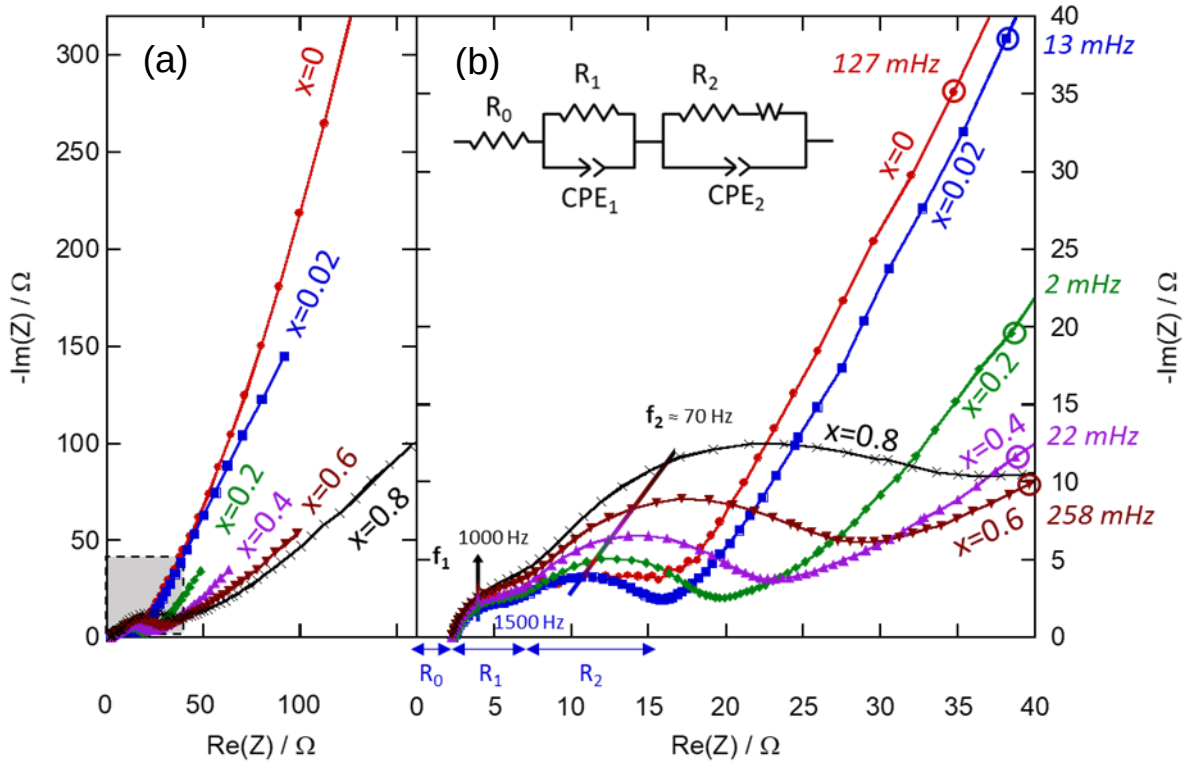

Figure 9. (a) Impedance spectra for discharged γ-$Na_xV_2O_5$ electrodes ($0 \leq x < 1$) (for x = 0, the spectrum is cut). Right graph (b) is a magnification of left graph, corresponding to the grey part.

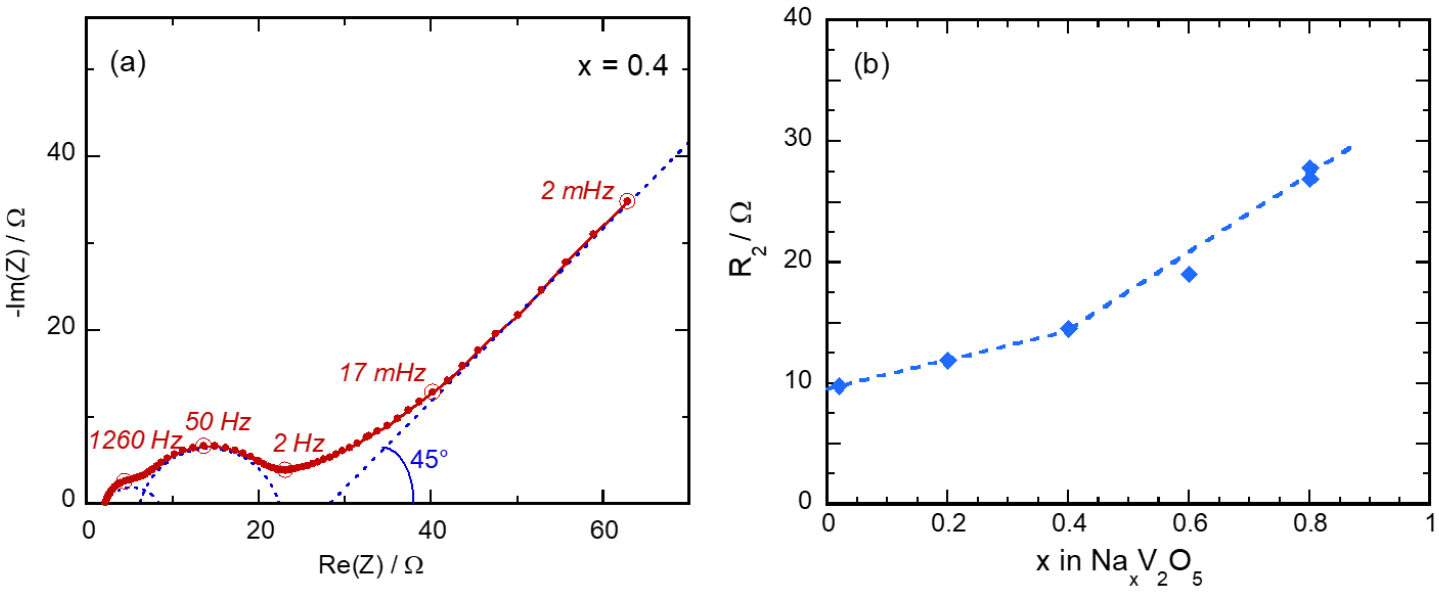

Figure 10. (a) Nyquist diagram for γ-$Na_{0.4}V_2O_5$ (b) Evolution of the charge transfer resistance (R_2)

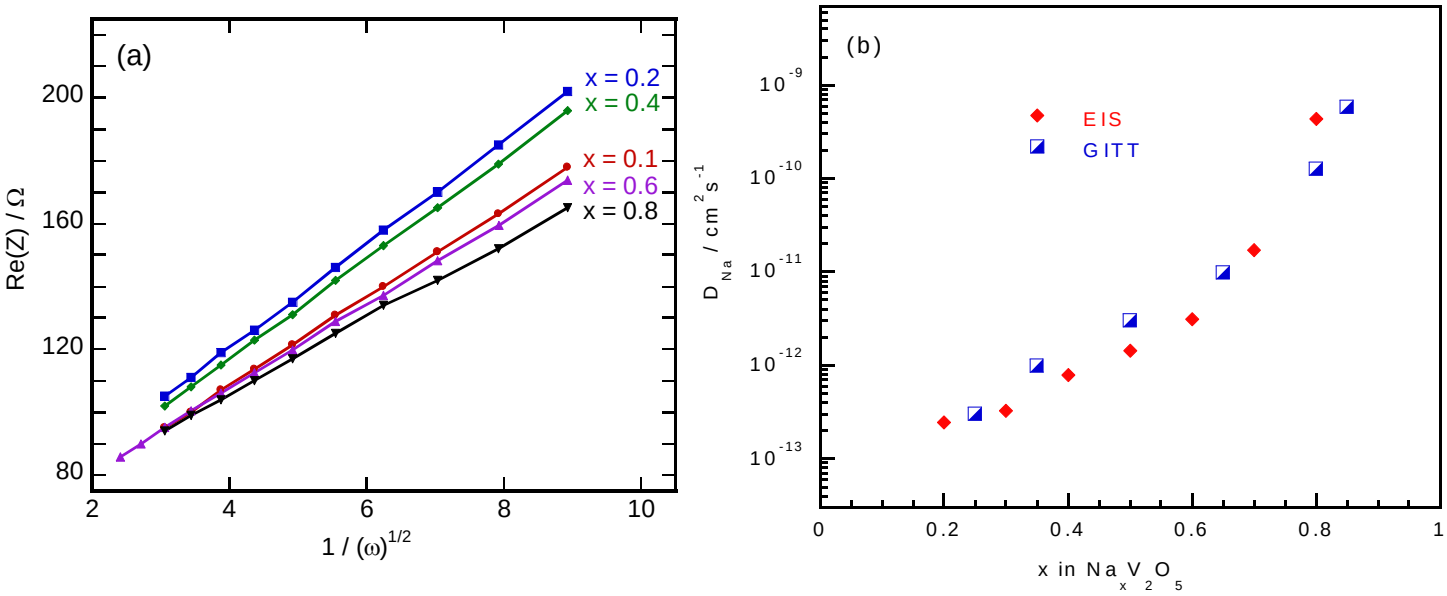

Figure 11. Evolution of (a) the Warburg prefactor and (b) the apparent chemical diffusion coefficient D_{Na} as a function of x ($0 < x < 1$) in γ-$Na_xV_2O_5$ obtained from EIS and GITT measurements.

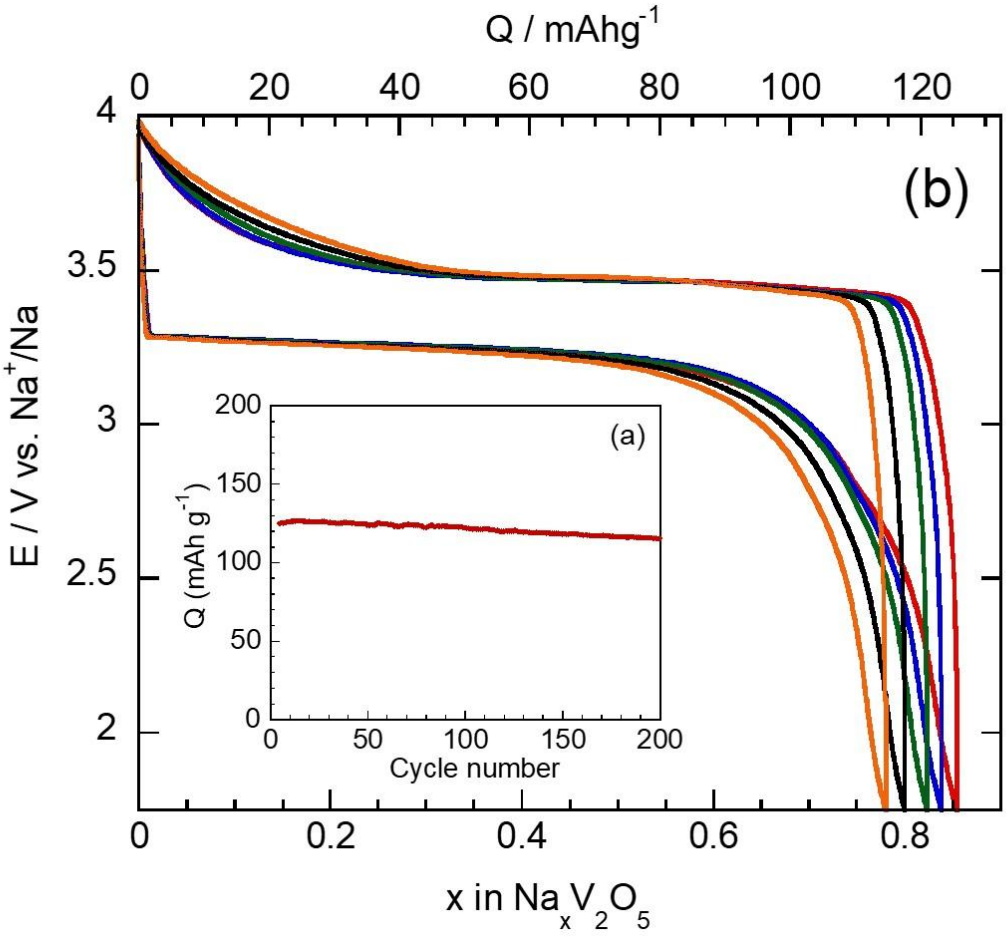

Figure 12. (a) Selected cycling galvanostatic curves (20th, 50th, 100th, 150th and 200th cycles) for γ'-polyol in 1 mol L^{-1} $NaClO_4$-PC-2 vol. % FEC in the 4V – 1.75 V potential range with a current density of 147 mA g^{-1} (1 C). (b) inset: Evolution of the discharge capacity as a function of the cycle number.